Subspace Projection Attention Network for GPR Heterogeneous Clutter Removal

Yanjie Cao, Xiaopeng Yang, *Senior Member, IEEE*, Conglong Guo, Dong Li, *Senior Member, IEEE*, Peng Yin, and Tian Lan, *Member, IEEE*

***Abstract*—Clutter removal in ground-penetrating radar (GPR) based on deep learning has been studied in recent years. However, existing methods are primarily designed for homogeneous background conditions and utilize only local spatial information via the convolution operation. In order to solve these issues, a subspace projection attention (SPA) network is proposed for GPR heterogeneous clutter removal in this article. First, a heterogeneous concrete dataset based on a numerical model with randomly placed aggregates is constructed, which incorporates the complex electromagnetic propagation process accurately to improve the effectiveness for heterogeneous clutter removal. In addition, the clutter basis learning neural network is designed by integrating the SPA module into the skip connection paths of U-Net architecture. By learning the subspace basis vectors adaptively, the SPA exploits both local and global spatial information to extract target features precisely. At the same time, the feature maps are projected to the target subspace to remove heterogeneous clutter features. Finally, the performance and effectiveness of proposed method are validated by simulations and experiments.**

***Index Terms*—Clutter removal, deep learning, ground-penetrating radar (GPR), heterogeneous clutter, subspace projection.**

I. Introduction

GROUND-PENETRATING radar (GPR) is one of the most widely used nondestructive detection technology, with applications in various fields, including civil engineering, transportation, mineral exploration, and military target detection [1]. However, during the application of high-frequency electromagnetic waves for detection, it has been observed that strong background clutter significantly impacts the detection and identification of targets. This clutter takes various forms, such as antenna direct coupled waves, reflected waves from the dielectric surface, and scattered waves from homogeneous and heterogeneous materials [2].

Conventional-model-based methods for clutter removal have been extensively studied, including mean subtraction, subspace-based methods, dictionary learning (DL) methods, and methods based on low-rank and sparse matrix decomposition (LRSD). Methods, such as mean subtraction or median subtraction method [3], [4], utilize the horizontal similarity of direct waves and surface reflected waves to remove clutter; subspace-based methods, including singular value decomposition [5], [6], [7], principle component analysis [8], and independent component analysis [9], [10], decompose B-scan data into clutter and target components and reconstruct the target subspace by selecting target components. However, in scenarios with multiple targets or heterogeneous clutter, targets and clutter often exist in the same component, resulting in the inability to completely separate targets from clutter. Besides, methods based on DL [11] and morphological component analysis [12] use different dictionaries to sparsely represent the clutter and target components of B-scans. But these methods have high algorithm complexity and lose the target information with inappropriate dictionary choices. The method based on LRSD theory treats the B-scan data as the sum of low-rank matrix and sparse matrix [13]. Low-rank matrices contain clutter, while sparse matrices contain target responses. Optimization of LRSD problems separates these two matrices revealing the target response. Representatives include robust principle component analysis (RPCA) [14], [15], robust nonnegative matrix factorization (RNMF) [16], and go decomposition [17] [18], [19]. However, optimal performance is dependent on the selection of regularization parameters. In short, traditional methods like LRSD have limitations, such as; 1) they have fixed models and require manual adjustments of parameters, or 2) high computational costs during iterative optimization, and 3) residual clutter when applied to complex heterogeneous concrete scenarios [20].

In recent years, deep-learning methods have shown exceptional feature learning capacity [21], [22], [23]. In terms of GPR clutter removal, a dual network implements unsupervised

Manuscript received 11 June 2023; revised 15 September 2023, 17 November 2023, and 21 December 2023; accepted 11 January 2024. Date of publication 17 January 2024; date of current version 1 February 2024. This work was supported in part by the National Natural Science Foundation of China under Grant 62101042, Grant 61860206012, and Grant 61901441; in part by the Natural Science Foundation of Chongqing under Grant cstc2021jcyj-msxmX0339; and in part by the Defense Industrial Technology Development Program under Grant JCKY2021906B002. *(Corresponding author: Tian Lan.)*

Yanjie Cao, Xiaopeng Yang, Conglong Guo, and Tian Lan are with the Beijing Institute of Technology Chongqing Innovation Center, Chongqing 401120, China, and also with the School of Information and Electronics, Beijing Institute of Technology, Beijing 100081, China (e-mail: caoyanjie@bit.edu.cn; xiaopengyang@bit.edu.cn; conglongguo@bit.edu.cn; tlan@bit.edu.cn).

Dong Li is with the School of Microelectronics and Communication Engineering, Chongqing University, Chongqing 400044, China (e-mail: lidongcuit@126.com).

Peng Yin is with the School of Cyber Security, University of Chinese Academy of Sciences, Beijing 100049, China, and also with the Defence Industry Secrecy Examination and Certification Center, Beijing 100089, China (e-mail: yinpeng@iie.ac.cn).

Digital Object Identifier 10.1109/JSTARS.2024.3355213

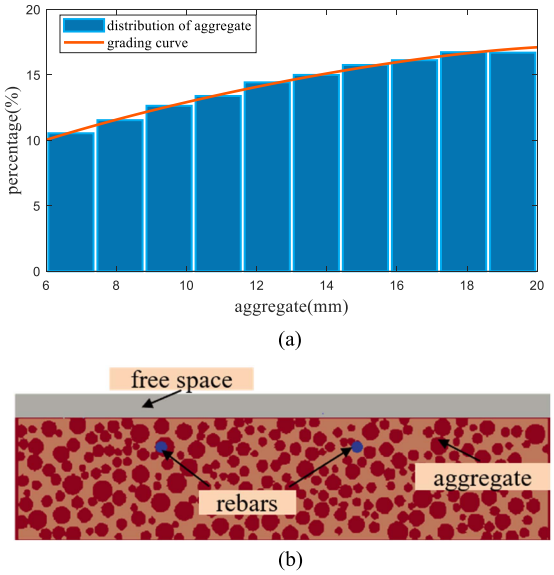

Fig. 1. Illustration of the heterogeneous model. (a) Distribution and grading curve of aggregate. (b) Visualization of distribution of individual components of concrete in the proposed heterogeneous model.

learning via pseudo tags based on RNMF outcomes [24]. Although the algorithm's speed has improved, its performance is similar to RNMF and it may be unstable and sensitive to the data especially for heterogeneous concrete scenarios. Other clutter removal techniques are based on the convolutional autoencoder [25], cGAN [26], and CR-Net [27] network architecture. Driven by a large amount of data, they have achieved the improvement of high signal to clutter ratio (SCR) with the strong supervised learning ability of the network. Temlioglu and Erer [25] proposed a GPR clutter suppression algorithm based on convolutional autoencoder, and the datasets are all based on the simulation data of homogeneous medium and heterogeneous soil medium, and the performance of the measured data is reduced. Ni et al. [26] designed a conditional generative adversarial network to remove clutter, and it can learn the mapping of clutter data and the corresponding clutter-free data in the training set. By training network data by constructing a dataset containing diverse real-world clutter, clutter-free images with good recovery target responses can be tried in [27]. However, in these methods, simulation B-scan models are mostly based on homogeneous materials and hence exhibit poor removal efficiency for heterogeneous clutter present in real scenarios like concrete conditions. Only the datasets used in [26] and [27] are based on the simulated target signal and the measured clutter signal stitched together to simulate real-world clutter but without considering the complex electromagnetic propagation process. However, noise and clutter from the heterogeneous concrete background can interfere with the features corresponding to the reflection of the object and make the identification of the reflection pattern in the B-scan difficult [35]. In addition, all these deep-learning-based methods are based on convolutional-operation-based network architecture, which utilizes only local spatial information from B-scans that fail to fully exploit global spatial information.

Therefore, we propose a clutter basis learning network for aggregate heterogeneity models to address the above issues. The contributions are as follows.

1) Unlike homogeneous simulated data or hybrid data in other data-driven approaches, a heterogeneous concrete dataset based on a random aggregate placement numerical model is constructed. This dataset takes into account the complex electromagnetic propagation process accurately while improving the effectiveness for heterogeneous clutter removal.
2) A clutter basis learning neural network (CBNet) for heterogeneous clutter removal is proposed. By combining subspace projection with data-driven methods, our method overcomes the traditional subspace methods' challenge to select target components effectively, while fully exploiting local and global spatial information of feature maps within the network.

The rest of this article is organized as follows. Section II provides further details on the aggregate dataset and CBNet network architecture. In Section III, extensive experiments are presented to demonstrate the advantages of our method in heterogeneous conditions. Finally, Section IV concludes this article.

II. Methodology

A. Simulated Dataset With Heterogeneous Clutter

The current datasets for clutter removal only consist homogeneous material scenes or simple heterogeneous soil models. As a result, it is difficult for data-driven methods to learn the complex and random heterogeneous clutter distribution observed in real echoes. However, when electromagnetic waves propagate in heterogeneous materials, they cause scattering and diffraction effects [28], which lead to clutter that always disguises the target responses.

Concrete is a heterogeneous composite material comprising coarse aggregate, fine aggregate, cement hydration slurry, microcracks, and pores [29], with aggregates mainly consisting of pebbles, crushed stones, etc. The presence of multiple composite materials results in random changes in their internal dielectric constant, leading to alterations in the electromagnetic characteristics of echoes. Studies have established that the weak reflection mode in concrete can be attributed to aggregate scattering [28] and it is directly related to the penetration depth of GPR in concrete, manifesting as heterogeneous clutter in B-scans.

To address these issues, we constructed a heterogeneous concrete dataset based on a random aggregate placement model. This model serves to train data-driven clutter removal methods, paving the way for more accurate and efficient clutter removal in real-world scenarios. In this numerical model, materials are represented through a matrix of electrical parameters (the permittivity, permeability, magnetic, and electric conductivity) at the nodes of cells. The effective permittivity ε_e is then described by an equation defined as follows [29]:

$$\varepsilon_e = \varepsilon + \frac{\sigma}{i\omega} = \varepsilon_e' - i\varepsilon_e'' \tag{1}$$

where ε_e' is the real part of the permittivity, ε_e'' is the imaginary part of the permittivity, σ is the conductivity, ω is the angular frequency, and i represents the complex imaginary number.

Random aggregate placement technology is a crucial component of concrete material strength calculation research. This method generates aggregates with shapes, sizes, and distributions that statistically match those found in actual concrete, based on a grading curve [as shown in Fig. 1(a)]. The grading curve describes the probability of any diameter of aggregate appearing in the cross-section as [31]

$$P_C(D) = P_K\left(1.065\left(\frac{D}{D_{\max}}\right)^{0.5} - 0.053\left(\frac{D}{D_{\max}}\right)^{4} - 0.012\left(\frac{D}{D_{\max}}\right)^{6} - 0.0045\left(\frac{D}{D_{\max}}\right)^{8} - 0.0025\left(\frac{D}{D_{\max}}\right)^{10}\right) \quad (2)$$

where $P_C(D)$ is the percentage of the cross-sectional circular area with a diameter less than D on the cross-section; P_K is the percentage of aggregate volume and total concrete volume; and $D_{\max}$ is the maximum particle size of the aggregate.

To generate aggregates that meet specific requirements [as shown in Fig. 1(a)], Monte Carlo sampling is used to obtain function values that simulate aggregate sizes. After that, the aggregates are placed in the simulation area according to an aggregate stacking rule. This rule is mainly determined by selecting the appropriate control parameters for the aggregate that conforms to the random distribution, such as center coordinates and radius, and checking whether the newly generated aggregate overlaps with previously created aggregates. During the placement process, the aggregates are generated as random polygons, and the proportion of their area to the total area is recorded. This allows for accurate monitoring of their distribution within the simulation area. The placement process terminates when the predetermined content value is met.

After the placement is completed, different electrical properties (e.g., the permittivity) are assigned to the aggregates and cement in concrete. These properties area used to generate a heterogeneous concrete B-scan with random characteristics using gprMax [33]. The simulation scenario is shown in Fig. 1(b). It consists of a two-dimensional area measuring 1.1 m $\times$ 0.3 m, with aggregate particle sizes ranging from 0.6 to 2 cm and varying aggregate contents of 30%, 40%, 50%, and 60% of the total concrete volume. In addition, the antenna center frequency is set at 2.6 GHz and is located above the surface of the concrete. The antenna is moved along the x-direction with a step of 1 cm. To simulate a synthetic dataset that is consistent with real-world data, concrete and aggregate permittivity are set at 7.0 and 8.5, respectively, and with a conductivity of 0.01 and 0.01 S/m. The radius of the target steel bar is randomly generated between 0.3 and 1.2 cm, with depths of burial ranging from 3 to 8 cm. The number of buried targets is randomly placed from 1 to 2 to simulate a single target scenario and a nonsingle target scenario.

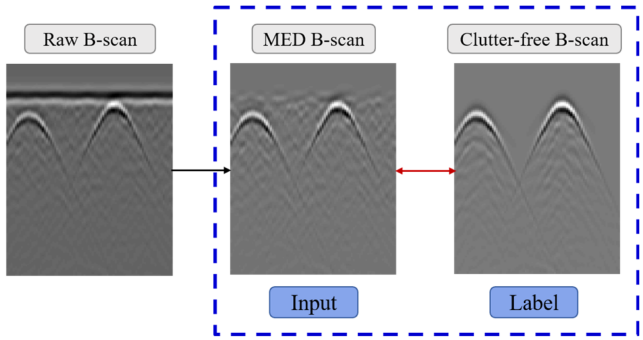

Fig. 2. Illustration of the raw B-scan, the corresponding median subtraction B-scan, and the clutter-free B-scan. The clutter-free B-scan is obtained by subtracting the background clutter from the raw B-scan.

The distribution of various components in the visualization scene of the proposed heterogeneous model is depicted in Fig. 1(b).

As shown in Fig. 2, the generated heterogeneous concrete B-scans are used as raw B-scans. In order to emphasize the heterogeneous clutter characteristics, the input of network is preprocessed using a clutter removal method based on median subtraction to obtain the MED B-scans. The results are shown in Fig. 2, and the formula for median subtraction is as follows:

$$\widetilde{s}(n,t) = s(n,t) - \mathrm{MED}_{k=1\ldots n}(s(k,t)) \quad (3)$$

where $s(n,t)$ represents the nth A-scan, $\mathrm{MED}(\cdot)$ represents the median operation, and $\widetilde{s}(n,t)$ is the nth A-scan data after median subtraction. In other words, the median subtraction method involves subtracting the median value of the row in which each element is located. This effectively removes the horizontal in-phase axis from the B-scan data and mitigates strong horizontal interference. By applying this operation, direct waves and flat surface reflection waves can be preliminarily removed, leaving behind residual surface reflected waves that resemble heterogeneous clutter. This approach also helps to address the issue of inconsistent surface reflected waves, which can arise during measurements of real-world scenes and comparisons with simulated data.

To obtain the necessary labels for training and evaluation, clutter-free B-scans are obtained by subtracting the background B-scans from the corresponding raw B-scans. Their corresponding cutter background B-scans are obtained by the same concrete condition but without burying objects as shown in Fig. 2.

B. Subspace Projection Attention Module

The subspace projection attention (SPA) [32] module utilizes the concept of image projection to learn basis vectors that can be used to reconstruct the image feature maps. In the case of the preprocessed B-scan input data, these basis vectors are generated to remove clutter and noise that are not relevant to the low-rank signal subspace (as shown in Fig. 3). However, the subspace basis in image processing is artificially constructed, and targets and clutter are often in a set of subspace basis that cannot be completely separated. Therefore, our method utilizes data-driven method to automatically learn subspace basis vectors and introduces attention mechanism to achieve the projection

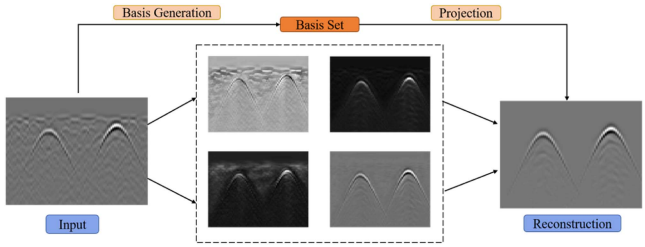

Fig. 3. Removal via subspace projection: CBNet learns to generate a set of basis for the signal subspace and by projecting the input into this space, signal can be enhanced after reconstruction for easy separation from clutter.

process. Besides, it also avoids the problem of traditional CNN networks only using local filtering to extract local spatial information [20]. It effectively utilizes global spatial information and better distinguishes the distribution of targets and clutter.

The schematic diagram of SPA is shown in Fig. 4. Assuming that $X_1, X_2 \in R^{H\times W\times C}$ are two feature maps of the same B-scan at different layers in the network. The low-level feature map is X_1 and the high-level feature map is X_2. H, W, C represent the height, width, and number of channels of the feature map, respectively. First, the subspace basis A is derived from X_1, X_2 through the function f_θ mapping generation

$$A = f_\theta(X_1, X_2) \tag{4}$$

where $A \in R^{HW\times r}$ is a matrix composed of basis vectors, r is the number of subspace basis vectors, and the function mapping $f_\theta : (R^{H\times W\times C}, R^{H\times W\times C}) \to R^{HW\times r}$ is generated from residual convolutional blocks. First, move X_1, X_2 along the channel dimension as $X \in R^{H\times W\times 2C}$ and input into a shallow residual convolutional block with output channel r. After that, the output dimension is converted to $HW \times r$. The basis vectors are obtained and the weights and biases of the basis vectors generated blocks are updated end-to-end during training.

After the basis vectors are generated, the projection section follows. It is known that the columns of matrix A are the basis vectors of the r-dimensional signal subspace Υ, and the B-scan image can be projected onto Υ by suitable orthogonal linear projection. Many basis vectors contain patterns that span evenly the entire image patch, attributed to the nonlocal correlation created by the SPA module. And the projection reconstructs the B-scan by combining the basis with globally determined coefficients. Assuming P_s is the orthogonal projection matrix of the target signal subspace and P_s can be calculated from A [34]

$$P_s = A(A^{\mathrm{T}}A)^{-1}A^{\mathrm{T}}. \tag{5}$$

The normalization term $(A^{\mathrm{T}}A)^{-1}$ is used to ensure that the basis vectors are orthogonal to each other. Finally, the image feature map X_1 can be reconstructed as Y in the target signal subspace

$$Y = P_s X_1. \tag{6}$$

In this article, the value of the number of subspace basis vectors is 16, which is less than the minimum channel number of 32 and most of the target features can be extracted. Setting K to 8 and 16 leads to comparable performance, and the SPA module might create a low-dimensional and classifiable subspace. Therefore, the subspace dimension K is a robust hyperparameter in a reasonable range. When the number of basis vectors K is set to 32, it does not converge. In this setting, as the number of channels in the first stage is also 32, the SPA module cannot work effectively as subspace projection since K equals to the full dimension size. If K equals 1, the information kept in the subspace is insufficient and cause significant target information loss in the skip connection [32].

C. Overall Network Architecture

The network architecture of CBNet is shown in Fig. 5, mainly consisting of U-Net neural network combined with SPA module. CBNet including encoders for compressed path and decoders for extended path and the SPA module is integrated into the skip connection process from low to high feature maps to remove clutter through adaptive projection. By providing subspace basis vectors close to the target, SPA can eliminate irrelevant and noisy responses generated by skip connections.

CBNet includes four encoders and four corresponding decoders. As shown in Fig. 5, each conv-block contains two 3×3 convolutional layers, and is followed by batch normalization operation and ReLU activation function. At the end of each encoder, the feature map is downsampled to a 1/2 scale using the max-pooling layer with a stride of 2, and upsampled to twice the scale using nearest neighbor interpolation before each decoder. Compared to traditional U-Net architectures that directly connect low-level and high-level feature maps at each decoder stage, the main difference of CBNet is that low-level features are projected by the SPA module before connection.

The low-level feature map is projected onto the signal subspace guided by upsampling high-level features, which can remove most irrelevant clutter and noise. Then, the projected features are connected with the original high-level features and output to the next decoder. Finally, the output of the decoder is passed through 1×1 The convolutional layer converts the number of channels to 1 to estimate clutter free data and outputs the results after removing clutter.

III. Experiments

In order to validate the proposed method, extensive experiments are conducted using GPR simulation data and real data from measured environments. The median subtraction method, the LRSD methods: RNMF and RPCA, the deep-leaning methods: CAE, cGAN, and CR-Net, and the proposed method: CBNet are implemented for comparison. The performance of the different methods is evaluated using quantitative metrics including peak signal-to-noise ratio (PSNR) and improvement factor (IF).

A. Performance Comparison on Simulated Data

PSNR is one of the quantitative metrics used in the article to evaluate the performance of different methods for simulated

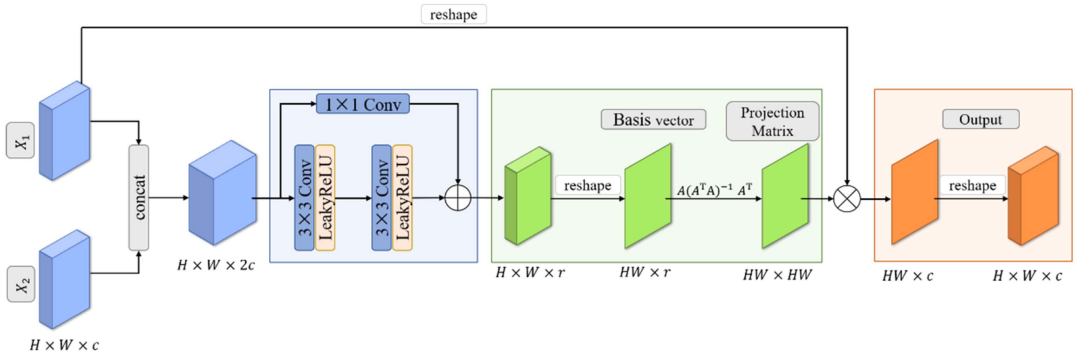

Fig. 4. Subspace projection attention (SPA) module.

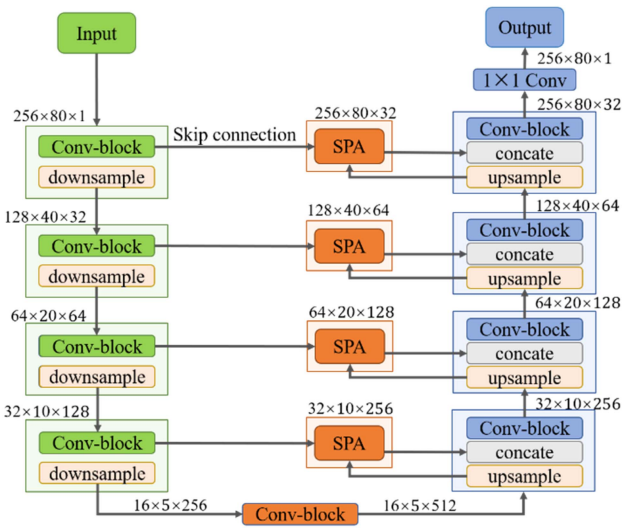

Fig. 5. Architecture of the CBNet network.

GPR data. PSNR can be calculated as follows:

$$\mathrm{PSNR(dB)} = 10 \cdot \log\left(\frac{1}{\mathrm{MSE}}\right) \tag{7}$$

$$\mathrm{MSE} = \frac{1}{M \times N}\sum_{i=1}^{N}\sum_{j=1}^{M}\left(g(i,j) - \widetilde{g}(i,j)\right)^2 \tag{8}$$

where $g(i,j)$ is the clutter free B-scan label and $\widetilde{g}(i,j)$ is the reconstructed B-scan image after clutter removal. MSE is mean square error; and M and N are dimensions of the B-scan. The larger PSNR values are, the better clutter removal performance is.

The simulation B-scan data are generated using the gprMax software based on the finite difference time-domain method, with a time window of 5 ns and trace number of 80 with a step of 1 cm. The targets in the data are ideal conductors PEC with radius ranging from 0.3 to 1.2 cm, buries at depths of 3 to 8 cm. Besides, the content of heterogeneous aggregate varies from 30% to 60%. The dataset including four types of aggregate content backgrounds, each contributing 50 sets of random heterogeneous backgrounds, and each set of backgrounds generates 20 kinds of targets, totaling $4 \times 50 \times 20 = 4000$ pairs of original data and clutter-free data (obtained through empty scene cancellation, as shown in Fig. 2). The training set and the test set were split at an 8:2 ratio. The network input is preprocessed data with median subtraction, while the label is target-only data under ideal clutter-free conditions (obtained by canceling with an empty scene without targets). The output is clutter removal results with only targets using CBNet implemented in PyTorch on NVIDIA 3090 GPU. The size of the B-scan data and their corresponding labels were adjusted to 256 × 80 for the training dataset. The network weights are initialized using a standard Gaussian function and 100 epochs are trained in total with a batch size of 4. We use Adam optimizer with an initial learning rate of 1e−4. The end-to-end training is performed based on the MSE loss function.

The simulation data completes the detection of PEC in heterogeneous concrete. A B-scan image obtained from the data is shown in Fig. 6(a) with a PEC target having a radius of 0.5 cm. Due to the high-intensity of antenna direct coupled waves, surface reflected waves, and heterogeneity of the concrete environment, the target echo signal is masked. Multiple clutter removal methods were applied and the results are shown in Fig. 6(b)–(h). First, the median subtraction method suppresses direct waves and flat surface reflection waves, but it is difficult to remove heterogeneous clutter. The robust nonnegative matrix decomposition method and the RPCA method based on the LRSD can be seen in the figure that the hyperbola of the target has been fully displayed, but there is still residual heterogeneous clutter near the target. The CAE and cGAN can both separate target component from the heterogeneous clutter background with a reduction of target information, thus have lower PSNR values than proposed methods. Compared with low rank sparse methods, the CR-Net method can further remove heterogeneous clutter. The proposed CBNet method has the best processing effect, improving target clarity and removing heterogeneous clutter while basically preserving the target signal. After that, the test dataset was also evaluated using PSNR and average performance metric as shown in Table I. Methods based on deep learning have a better performance than MED, RNMF, and RPCA, and the CBNet has the highest average PSNR.

In addition, the main reason for more clutter displayed below the hyperbola when using DL-based methods is the presence of clutter in clutter-free B-scan for training data. As shown in Fig. 2, the clutter-free B-scan is obtained by

TABLE I
IF RESULTS OF SIMULATION DATA

	MED	RNMF	RPCA	CAE	cGAN	CR-Net	CBNet
PSNR(↑)/dB	31.45	35.67	37.20	37.99	44.51	45.00	46.21

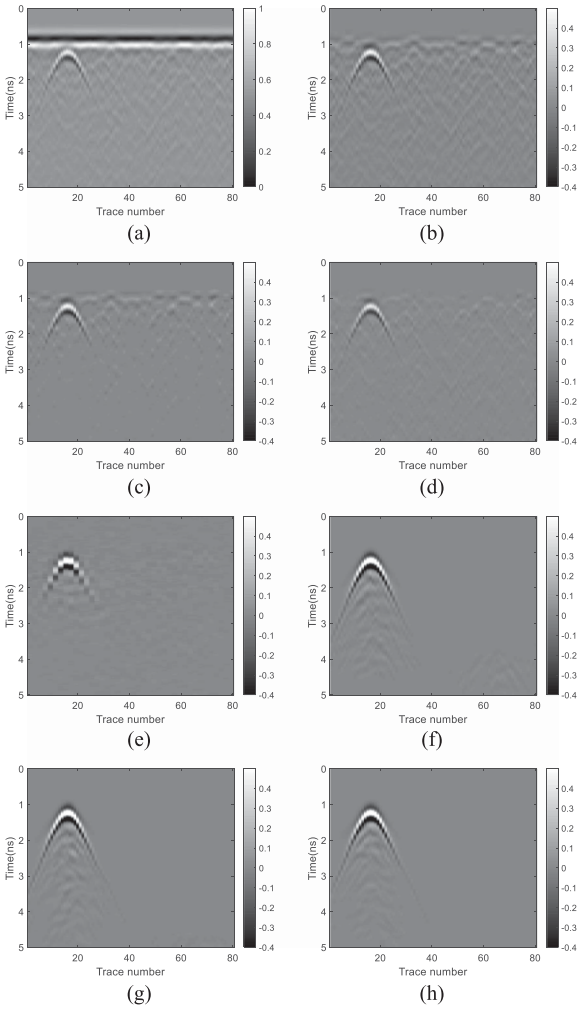

Fig. 6. Simulation B-scan data results. (a) Raw data. (b) MED. (c) RNMF. (d) RPCA. (e) CAE. (f) cGAN. (g) CR-Net. (h) CBNet.

subtracting the background clutter from the raw B-scan and their corresponding cutter background B-scans are obtained by the same concrete condition but without burying objects. The clutter from the heterogeneous concrete background can interfere with the features corresponding to the reflection of the object and make the reflection pattern in the B-scan different. Therefore, there seems to be more clutter displayed below the hyperbola, but it does not affect the effect of the DL-based methods.

B. Performance Comparison on Real Data

Due to the unavailability of clutter-free B-scans for real field data, IF is used to estimate the variation of SCR before and after clutter removal, and the SCR of B-scan data is

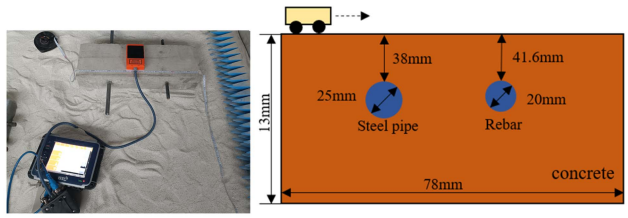

Fig. 7. (a) Schematic diagram of experimental scenarios and targets. (b) Illustration of the experimental scenarios.

defined as [30]

$$\mathrm{SCR} = \frac{N_c \sum\limits_{i \in \boldsymbol{R}_s} |\boldsymbol{X}(i)|^2}{N_s \sum\limits_{i \in \boldsymbol{R}_c} |\boldsymbol{X}(i)|^2} \tag{9}$$

where N_c and N_s are the number of pixels in the clutter area $\boldsymbol{R}_c$ and target area $\boldsymbol{R}_s$, respectively, $\boldsymbol{X}(i)$ are the ith pixel of $\boldsymbol{X}$. The IF can be defined by the following equation:

$$\mathrm{IF} = 10\log_{10}\left(\mathrm{SCR}_{\mathrm{after}}/\mathrm{SCR}_{\mathrm{before}}\right) \tag{10}$$

where $\mathrm{SCR}_{\mathrm{before}}$ and $\mathrm{SCR}_{\mathrm{after}}$ represent the signal-to-clutter ratio of the image before and after clutter removal.

Real data for detecting rebars in concrete are collected using the GSSI SIR4000 radar system with an antenna center frequency of 2600 MHz (as shown in Fig. 7). The targets include a steel pipe with a diameter of 25 mm and a rebar with a diameter of 20 mm, buried in the concrete medium. The obtained GPR image is shown in Fig. 8(a). It can be seen that the two horizontal lines represent the upper and lower surfaces of the concrete, respectively. In addition, there is visible heterogeneous clutter at the same time. Multiple clutter removal methods were applied, and the results are shown in Fig. 8(b)–(h). The comparison of performance metrics is shown in Table II. After median subtraction, there are still random heterogeneous clutter remaining. Although RNMF and RPCA can remove directly coupled waves and surface reflection waves, there are still many residual reflection waves that cannot be effectively processed for underground heterogeneous medium reflection waves. CAE and cGAN can both separate target component from the heterogeneous clutter background but with a reduction of target information, and they both have lower IF values than proposed methods. Although CR-Net excelled at suppressing surface reflections, it was marginally successful in addressing the issue of heterogeneous medium reflection waves. However, the CBNet architecture-based method exhibited enhanced performance by significantly reducing both surface and heterogeneous medium reflection waves, highlighting target information and demonstrating excellent IF values. These findings support the effectiveness of the proposed methodology.

TABLE II
IF RESULTS OF REAL DATA

	MED	RNMF	RPCA	CAE	cGAN	CR-Net	CBNet
IF(↑)/dB	13.55	15.07	14.41	16.63	19.34	17.05	22.84

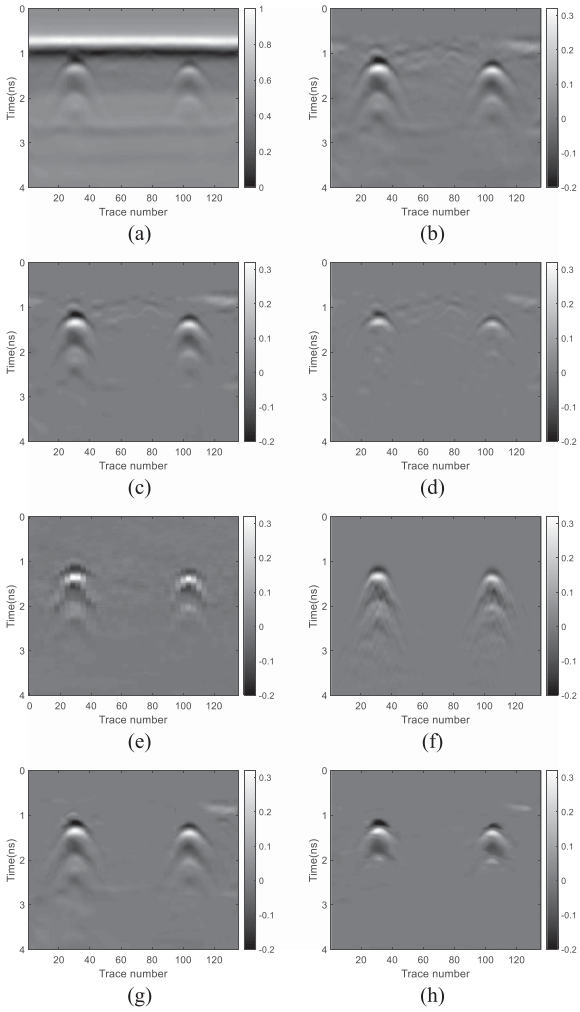

Fig. 8. Real B-scan data results. (a) Raw data. (b) MED. (c) RNMF. (d) RPCA. (e) CAE. (f) cGAN. (g) CR-Net. (h) CBNet.

To demonstrate the impact of the SPA module on clutter removal networks, we randomly selected an example from the test dataset and visualized the basis vectors in the same dimensions as the output. Of the 16 basis vectors, many contain patterns that span evenly the entire image patch, attributed to the nonlocal correlation created by the SPA module. And the projection reconstructs the B-scan by combining the basis with globally determined coefficients. As can be seen from the Fig. 9, most of the basis vectors highlight the target information due to the orthogonal linear projection, so feature maps can be projected onto the target subspace. The SPA module generates target subspace basis vectors through data-driven adaptive learning, which contain most of the target information and suppress clutter and noise that do not pertain to the generated basis set. Then, the feature maps are projected onto the corresponding subspace

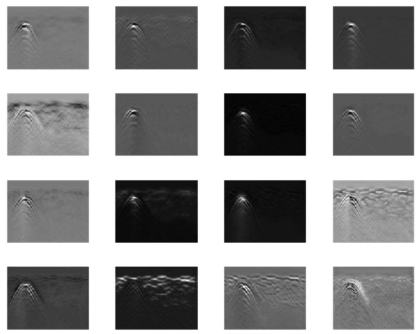

Fig. 9. Visualization result of the basis vectors that span the projection subspace ($K = 16$).

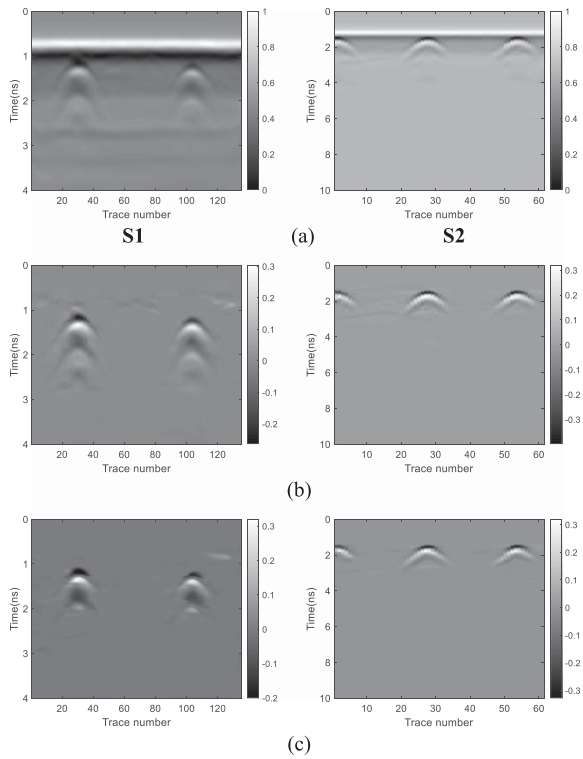

Fig. 10. Real B-scan data results. (a) Raw data. (b) U-Net. (c) CBNet.

to enhance the target signal, effectively utilizing global spatial information and better distinguishing the distribution of target and clutter. To verify its performance on real data, we compared CBNet to the base U-Net network architecture (Fig. 10). The CBNet performs superiorly in removing heterogeneous clutter due to the addition of the SPA module, as well as exhibiting higher IF values as Table III shows.

We have tested the proposed approach on different datasets with various levels of heterogeneous clutter and compare it with a wide range of existing methods to verify the robustness of the

TABLE III
IF RESULTS OF REAL DATA (DB)

	U-Net	CBNet
S1	20.68	22.84
S2	30.71	31.95

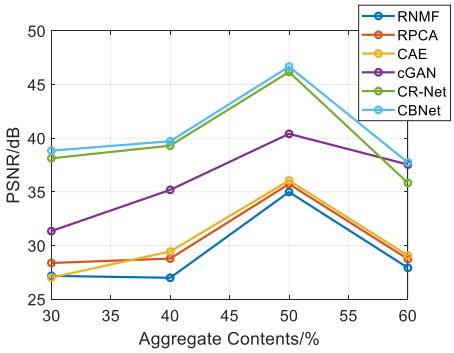

Fig. 11. PSNR values for different methods under different aggregate contents.

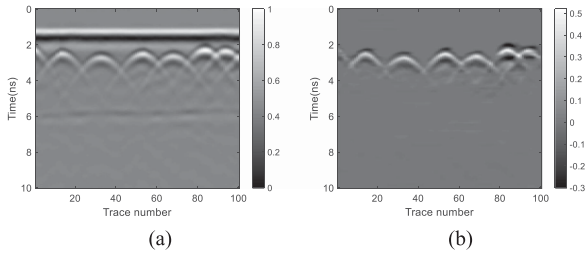

Fig. 12. Real B-scan data results for 1.6 GHz antenna. (a) Scene 1. (b) Result 1.

methods. As Fig. 11 shows, the aggregate contents are varied from 30% to 60% of the total concrete volume and comparison methods include RNMF, RPCA, CAE, cGAN, CR-Net, and the proposed CBNet. It can be seen that RNMF and RPCA, as traditional low-rank sparse decomposition methods, have poor suppression effect on heterogeneous clutter and have lower PSNR, while the method based on deep learning performs better, among which, our method can have the best performance regardless of heterogeneous clutter at all levels, and PSNR is the highest. Therefore, it is proved that the proposed method has strong robustness.

Furthermore, to verify the generalization ability of the network, we changed the antenna center frequency to 1.6 GHz and the B-scan data are shown in Fig. 12. It is a concrete wall in a real-world lab scene and the results presented in Fig. 12(b) indicate that the proposed CBNet can achieve good clutter removal effects. In addition, we tested another set of concrete data with an effective permittivity of about 4.5 and a rebar radius of about 13 mm, in which the electrical information of concrete material and the size of targets are different from the strategy used in the simulation scenario. It can be seen from Fig. 13 that the proposed method can still remove most of the clutter, showing a clear target hyperbolic signal.

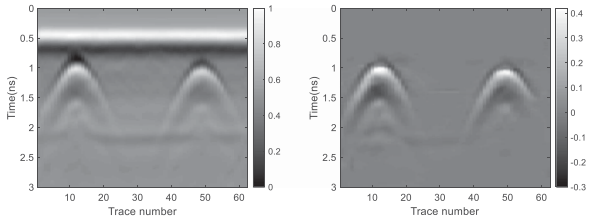

Fig. 13. Real B-scan data results for new scenario. (a) Scene 2. (b) Result 2.

TABLE IV
TRAINING AND TEST TIME FOR DIFFERENT NETWORKS

	CAE	cGAN	CR-Net	CBNet
Training Time/s(GPU)	2647	6633	1634	6263
Test Time/s(CPU)	0.5	0.16	0.75	1

Table IV lists the training time and test time comparison for different methods. Due to the combination of the subspace projection module, the CBNet network has a superior clutter removal capability as the training time increases, but this has little impact on the test time. All the test time is within 1 s in CPU. After this work, we will investigate network lightweighting efforts to reduce the training and test time of the proposed method.

IV. CONCLUSION

In this article, we propose a novel CBNet for removing heterogeneous clutter in GPR. A heterogeneous concrete dataset containing aggregate scattering is built to train the network. This approach reduces the requirement for field data and improves the effectiveness of the dataset. Moreover, CBNet combines subspace projection module and data-driven methods for the first time in GPR clutter removal, solving the challenge of traditional subspace methods that often encounter difficulties in selecting target components. In addition, CBNet fully exploits local and global spatial information available from feature maps in the network. Extensive experiments show that when the echo signal contains target signal and heterogeneous clutter, our method can provide high-definition target signal and obtain high IF values which is superior to the existing methods. Moreover, experiments concerning multitarget scenarios validate the generalization ability of our method, underscoring its potential applications in practical environments.

REFERENCES

[1] J. D. J. Daniels, D. J. Gunton, and H. F. Scott, "Introduction to subsurface radar," *IEE Proc. F (Commun., Radar Signal Process.). IET Digit. Library*, vol. 135, no. 4, pp. 278–320, Aug. 1988.
[2] H. Brunzell, "Detection of shallowly buried objects using impulse radar," *IEEE Trans. Geosci. Remote Sens.*, vol. 37, no. 2, pp. 875–886, Mar. 1999.
[3] A. M. Zoubir, I. J. Chant, C. L. Brown, B. Barkat, and C. Abeynayake, "Signal processing techniques for landmine detection using impulse ground penetrating radar," *IEEE Sensors J.*, vol. 2, no. 1, pp. 41–51, Feb. 2002.
[4] R. Solimene, A. Cuccaro, A. Dell'Aversano, I. Catapano, and F. Soldovieri, "Ground clutter removal in GPR surveys," *IEEE J. Sel. Topics Appl. Earth Observ. Remote Sens.*, vol. 7, no. 3, pp. 792–798, Mar. 2014.

[5] G. Chen, L. Fu, K. Chen, C. D. Boateng, and S. Ge, "Adaptive ground clutter reduction in ground-penetrating radar data based on principal component analysis," *IEEE Trans. Geosci. Remote Sens.*, vol. 57, no. 6, pp. 3271–3282, Jun. 2019.
[6] F. Nan, S. Zhou, Y. Wang, F. Li, and W. Yang, "Reconstruction of GPR signals by spectral analysis of the SVD components of the data matrix," *IEEE Geosci. Remote Sens. Lett.*, vol. 7, no. 1, pp. 200–204, Jan. 2010.
[7] T. M. Grzegorczyk, B. Zhang, and M. T. Cornick, "Optimized SVD approach for the detection of weak subsurface targets from ground-penetrating radar data," *IEEE Trans. Geosci. Remote Sens.*, vol. 51, no. 3, pp. 1635–1642, Mar. 2013.
[8] J. Q. Shen, H. Z. Yan, and C. Z. Hu, "Auto-selected rule on principal component analysis in ground penetrating radar signal denoising," *Chin. J. Radio Sci.*, vol. 25, no. 1, pp. 83–87, Feb. 2010.
[9] F. Abujarad and A. Omar, "Comparison of independent component analysis (ICA) algorithms for GPR detection of non-metallic land mines," *Image Signal Process. Remote Sens.*, vol. 6365, pp. 362–373, Sep. 2006.
[10] B. Karlsen, J. Larsen, H. B. D. Sorensen, and K. B. Jakobsen, "Comparison of PCA and ICA based clutter reduction in GPR systems for anti-personal landmine detection," in *Proc. IEEE 11th Signal Process. Workshop Statist. Signal Process.*, 2001, pp. 146–149.
[11] Z.-K. Ni, J. Pan, C. Shi, S. Ye, D. Zhao, and G. Fang, "DL-based clutter removal in migrated GPR data for detection of buried target," *IEEE Geosci. Remote Sens. Lett.*, vol. 19, 2022, Art. no. 3507205.
[12] Y. Zhou and W. Chen, "MCA-based clutter reduction from migrated GPR data of shallowly buried point target," *IEEE Trans. Geosci. Remote Sens.*, vol. 57, no. 1, pp. 432–448, Jan. 2019.
[13] D. Kumlu and I. Erer, "Clutter removal in GPR images using nonnegative matrix factorization," *J. Electromagn. Waves Appl.*, vol. 32, no. 16, pp. 2055–2066, Jun. 2018.
[14] X. Song, D. Xiang, K. Zhou, and Y. Su, "Improving RPCA-based clutter suppression in GPR detection of antipersonnel mines," *IEEE Geosci. Remote Sens. Lett.*, vol. 14, no. 8, pp. 1338–1342, Aug. 2017.
[15] D. Kalika, M. T. Knox, L. M. Collins, P. A. Torrione, and K. D. Morton, "Leveraging robust principal component analysis to detect buried explosive threats in handheld ground-penetrating radar data," *Proc. SPIE*, vol. 9454, May 2015, Art. no. 94541D.
[16] D. Kumlu and I. Erer, "Improved clutter removal in GPR by robust nonnegative matrix factorization," *IEEE Geosci. Remote Sens. Lett.*, vol. 17, no. 6, pp. 958–962, Jun. 2020.
[17] X. Song, D. Xiang, K. Zhou, and Y. Su, "Fast prescreening for GPR antipersonnel mine detection via go decomposition," *IEEE Geosci. Remote Sens. Lett.*, vol. 16, no. 1, pp. 15–19, Jan. 2019.
[18] D. Kumlu and I. Erer, "GPR clutter reduction by robust orthonormal subspace learning," *IEEE Access*, vol. 8, pp. 74145–74156, 2020.
[19] Z.-K. Ni, S. Ye, C. Shi, C. Li, and G. Fang, "Clutter suppression in GPR B-scan images using robust autoencoder," *IEEE Geosci. Remote Sens. Lett.*, vol. 19, 2022, Art. no. 3500705.
[20] H. Sun, K. Zheng, M. Liu, C. Li, D. Yang, and J. Li, "Hyperspectral image mixed noise removal using a subspace projection attention and residual channel attention network," *Remote Sens.*, vol. 14, no. 9, 2022, Art. no. 2071.
[21] M. Moalla, H. Frigui, A. Karem, and A. Bouzid, "Application of convolutional and recurrent neural networks for buried threat detection using ground penetrating radar data," *IEEE Trans. Geosci. Remote Sens.*, vol. 58, no. 10, pp. 7022–7034, Oct. 2020.
[22] M.-T. Pham and S. Lefevre, "Buried object detection from B-scan ground penetrating radar data using faster-RCNN," in *Proc. IEEE Int. Geosci. Remote Sens. Symp.*, 2018, pp. 6804–6807.
[23] P. Bestagini, F. Lombardi, M. Lualdi, F. Picetti, and S. Tubaro, "Landmine detection using autoencoders on multipolarization GPR volumetric data," *IEEE Trans. Geosci. Remote Sens.*, vol. 59, no. 1, pp. 182–195, Jan. 2021.
[24] H. Zhou, Y. Wang, Q. Liu, and Y. Wang, "RNMF-guided deep network for signal separation of GPR without labeled data," *IEEE Geosci. Remote Sens. Lett.*, vol. 19, 2022, Art. no. 3507705.
[25] E. Temlioglu and I. Erer, "A novel convolutional autoencoder-based clutter removal method for buried threat detection in ground-penetrating radar," *IEEE Trans. Geosci. Remote Sens.*, vol. 60, 2022, Art. no. 5103313.
[26] Z.-K. Ni, C. Shi, J. Pan, Z. Zheng, S. Ye, and G. Fang, "Declutter-GAN: GPR B-scan data clutter removal using conditional generative adversarial nets," *IEEE Geosci. Remote Sens. Lett.*, vol. 19, 2022, Art. no. 4023105.
[27] H.-H. Sun, W. Cheng, and Z. Fan, "Learning to remove clutter in real-world GPR images using hybrid data," *IEEE Trans. Geosci. Remote Sens.*, vol. 60, 2022, Art. no. 5113714.
[28] J. Lachowicz and M. Rucka, "A concept of heterogeneous numerical model of concrete for GPR simulations," in *Proc. 9th Int. Workshop Adv. Ground Penetrating Radar*, 2017, pp. 1–4.
[29] S. Laurens, J. P. Balayssac, J. Rhazi, G. Klysz, and G. Arliguie, "Nondestructive evaluation of concrete moisture by GPR: Experimental study and direct modeling," *Mater. Struct.*, vol. 38, no. 283, pp. 827–832, 2005.
[30] L. Liu, Z. Wu, H. Xu, B. Wang, and J. Li, "GPR clutter removal based on factor group-sparse regularization," *IEEE Geosci. Remote Sens. Lett.*, vol. 19, 2022, Art. no. 3509305.
[31] J. Walraven and H. Reinhardt, "Theory and experiments on the mechanical behaviour of cracks in plain and reinforced concrete subjected to shear loading," *HERON*, vol. 26, pp. 26–35, 1981.
[32] S. Cheng, Y. Wang, H. Huang, D. Liu, H. Fan, and S. Liu, "NBNet: Noise basis learning for image denoising with subspace projection," in *Proc. IEEE/CVF Conf. Comput. Vis. Pattern Recognit.*, 2021, pp. 4896–4906.
[33] C. Warren, A. Giannopoulos, and I. Giannakis, "gprMax: Open source software to simulate electromagnetic wave propagation for ground penetrating radar," *Comput. Phys. Commun.*, vol. 209, pp. 163–170, 2016.
[34] C. D. Meyer, "Matrix analysis and applied linear algebra book and solutions manual," *Soc. Ind. Appl. Math.*, Philadelphia, PA, USA, 2000.
[35] Q. Dai, Y. H. Lee, H.-H. Sun, G. Ow, M. L. M. Yusof, and A. C. Yucel, "DMRF-UNet: A two-stage deep learning scheme for GPR data inversion under heterogeneous soil conditions," *IEEE Trans. Antennas Propag.*, vol. 70, no. 8, pp. 6313–6328, Aug. 2022.

Yanjie Cao was born in Taiyuan, Shanxi, China, in 1999. He received the B.S. degree in electronic information engineering from the Xidian University, Shaanxi, China, in 2021. He is currently working toward the M.S. degree in information and communication engineering with the Beijing Institute of Technology, Beijing, China.

His research interests include clutter removal for ground-penetrating radar.

Xiaopeng Yang (Senior Member, IEEE) received the B.S. and M.S. degrees in electronic and communication engineering from the Xidian University, Xi'an, China, and the Ph.D. degree from the Tohoku University, Sendai, Japan.

He is currently a Professor with the School of Information and Electronics, Beijing Institute of Technology (BIT), Beijing, China. He was a Postdoctoral Research Fellow with the Tohoku University, and a Research Associate with the Syracuse University, Syracuse, NY, USA, from 2007 to 2010. Since 2010, he has been working with the BIT. He has authored/coauthored more than 70 journal papers and 100 conference papers, granted 18 Chinese patents, and more than 10 invited talks in academic conferences. His research interests include radar signal processing, through-the-wall radar, and ground-penetrating radar.

Dr. Yang is a Fellow of Chinese Institute of Electronics (CIE). He is the BOG of Chinese Radar Industry Association, the Deputy Director of the CIE Radar society, BOG of IEEE AESS, member of IEEE AESS Radar System Panels, the General Chair of IET International Radar Conference 2020 and 2023, and TPC Chair of IEEE ICSIDP 2019. He was the recipient of the first Prize of CASC Science and Technology Progress Award, the outstanding scientific researcher of CIE, the Journal paper award in Chinese Electronics, the paper awards of IEEE and IET International Conference and National Radar Conference, and excellent award of editorial board of modern radar.

Conglong Guo received the B.S. degree in information and communication engineering from the Beijing Institute of Technology, Beijing, China, in 2021. He is currently working toward the M.S. degree in information and communication engineering with the Beijing Institute of Technology, Beijing, China.

His research interests include electromagnetic inversion in ground-penetrating radar and machine learning.

Dong Li (Senior Member, IEEE) was born in Inner Mongolia, China, in 1983. He received the B.S. degree in automation from the Chengdu University of Information Technology, Chengdu, China, in 2007, the M.S. degree in signal processing from the Sichuan University, Chengdu, China, in 2010, and the Ph.D. degree in signal and information processing from the National Laboratory of Radar Signal Processing, Xidian University, Xi'an, China, in 2014.

He is currently a Professor with the School of Microelectronics and Communication Engineering, Chongqing University, Chongqing, China. His research interests include target detection and tracking, and parameter estimation.

Peng Yin was born in 1989. He received the B.S. and M.S. degrees in information and communication engineering from the Beijing Institute of Technology, Beijing, China, in 2013 and 2017, respectively. He is currently working toward the Ph.D. degree in cyberspace security with the School of Cyber Security, University of Chinese Academy of Sciences, Beijing, China.

He is currently working as an Associate Research Fellow with the Defence Industry Secrecy Examination and Certification Center. His research interests include electromagnetic cyberspace security, integrated sensing and communication technology, signal detection, and recognition technology.

Tian Lan (Member, IEEE) received the B.S. degree in electromagnetic fields and wireless technology and the M.S. degree in electromagnetic fields and microwave technology from the University of Electronic Science and Technology of China, Chengdu, China, in 2011 and 2014, respectively, and the Ph.D. degree in electromagnetic fields and microwave technology from the Xiamen University, Xiamen, China, in 2020.

From 2019 to 2020, he was a Senior Antenna Engineer with the OPPO. Company Ltd, Dongguan, China. He is currently an Associate Researcher with the Beijing Institute of Technology, Beijing, China. His research interests include electromagnetic inversion in ground-penetrating radar and through the wall radar.